AGU ADVANCING EARTH AND SPACE SCIENCE

JAMES | Journal of Advances in Modeling Earth Systems®

RESEARCH ARTICLE
10.1029/2022MS003280

Key Points:

- Three different scale analysis methods for unstructured triangular grids are presented and discussed
- Fourier spectra after interpolation of fields should be applied with caution especially for dissipation power spectra
- Scale analysis via indicator functions does not rely on interpolation and can be applied to non-smooth, unstructured data

Correspondence to:
S. Juricke,
sjuricke@awi.de

Citation:
Juricke, S., Bellinghausen, K., Danilov, S., Kutsenko, A., & Oliver, M. (2023). Scale analysis on unstructured grids: Kinetic energy and dissipation power spectra on triangular meshes. *Journal of Advances in Modeling Earth Systems*, *15*, e2022MS003280. https://doi.org/10.1029/2022MS003280

Received 30 JUN 2022
Accepted 14 DEC 2022

Scale Analysis on Unstructured Grids: Kinetic Energy and Dissipation Power Spectra on Triangular Meshes

S. Juricke[1,2], K. Bellinghausen[2], S. Danilov[1,2], A. Kutsenko[1,3], and M. Oliver[1,3]

[1]Department of Mathematics and Logistics, Jacobs University, Bremen, Germany, [2]Alfred Wegener Institute for Polar and Marine Research, Bremerhaven, Germany, [3]Mathematical Institute for Machine Learning and Data Science, KU Eichstätt–Ingolstadt, Ingolstadt, Germany

Abstract Fourier spectra are powerful tools to analyze the scale behavior of turbulent flows. While such spectra are mathematically based on regular periodic data, some state-of-the-art ocean and climate models use unstructured triangular meshes. Observational data is often also available only in an unstructured fashion. In this study, scale analysis specifically for the output of models with triangular meshes is discussed and the representable wavenumbers for Fourier analysis are derived. Aside from using different interpolation methods and oversampling prior to the computation of Fourier spectra, we also consider an alternative scale analysis based on the Walsh–Rademacher basis, that is, indicator functions. It does not require interpolation and can be extended to general unstructured meshes. A third approach based on smoothing filters which focus on grid scales is also discussed. We compare these methods in the context of kinetic energy and dissipation power of a turbulent channel flow simulated with the sea ice-ocean model FESOM2. One simulation uses a classical viscous closure, another a new backscatter closure. The latter is dissipative on small scales, but anti-dissipative on large scales leading to more realistic flow representation. All three methods clearly highlight the differences between the simulations as concerns the distribution of dissipation power and kinetic energy over scales. However, the analysis based on Fourier transformation is highly sensitive to the interpolation method in case of dissipation power, potentially leading to inaccurate representations of dissipation at different scales. This highlights the necessity to be cautious when choosing a scale analysis method on unstructured grids.

Plain Language Summary To better understand the physical processes that drive and define the circulation in our oceans, it is necessary to analyze the temporal and spatial scales on which these processes act. The classical method to investigate the spatial scale behavior is Fourier analysis which splits any given data into waves of different amplitudes and wavelengths. Mathematically this requires data on an equidistantly spaced grid. However, many ocean models apply triangular or other irregular grids for their computations of oceanic flows. In this study, we describe the advantages and disadvantages of applying Fourier analysis for models that use triangular meshes, with prior interpolation of data to regularly spaced rectangular meshes. We also introduce two other methods that can analyze the distribution of kinetic energy and kinetic energy dissipation across scales without interpolation. The results show that one needs to be very careful when choosing a specific scale analysis and, potentially, an interpolation method for triangular grids, especially when it comes to analyzing the process of kinetic energy dissipation.

1. Introduction

Improving our understanding of scaling laws in geophysical fluid dynamics is of fundamental importance when analyzing crucial scale interactions or, in the context of model development, when designing parameterizations for the unresolved subgrid scales (e.g., Danilov et al., 2019). Scale analysis of turbulent flows is a classical approach to investigate the dynamics simulated by numerical models (e.g., Schubert et al., 2020; Soufflet et al., 2016) and to compare them to observational estimates (e.g., Wang et al., 2019). A variety of methods is available to separate out specific scales in multiscale flows (e.g., Kumar & Foufoula-Georgiou, 1997) or to coarse-grain or filter the information from smaller scales to larger scales (e.g., Aluie, 2019; Aluie et al., 2018; Berloff, 2018; Grooms et al., 2021; Sadek & Aluie, 2018). These methods generally involve spatial or temporal filters to remove specific scales, or projectors which split the data into a hierarchy of Hilbert-subspaces. Such coarse-graining is less straight forward on unstructured triangular meshes, but can nevertheless be designed to achieve conservation of certain quantities or derivatives (Patching, 2022).

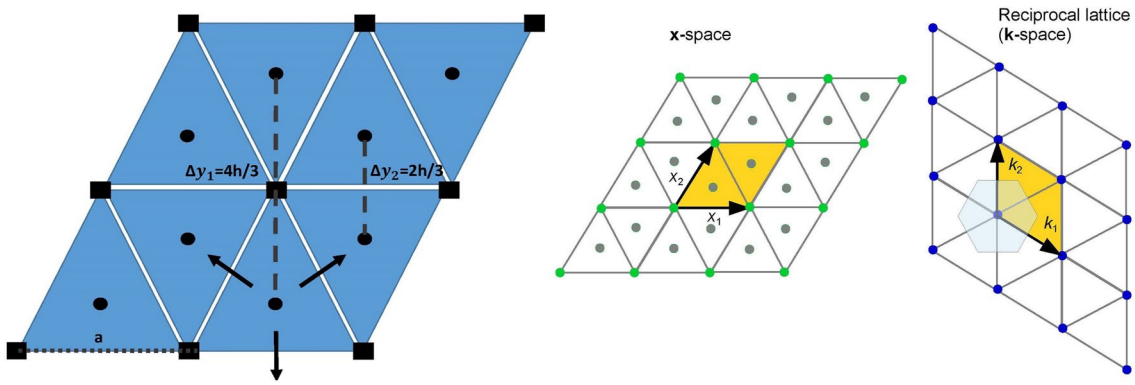

Figure 1. (left) Regular equilateral triangular mesh with vertices (black squares) and centroids (black circles). There are two types of triangles (pointing upward and downward). The distances between centroids in the *y*-direction alternate between 2*h*/3 and 4*h*/3, where *h* is the height (dashed lines), creating a geometrical pattern in data placed at centroids. The side length of the equilateral triangles is *a* (dotted line). (right) Triangular mesh and its reciprocal lattice in ***k***-space. Unit cells are shown in orange. The first Brillouin zone is the Voronoi hexagon around an origin point of the reciprocal lattice. Small green and blue circles correspond to $\boldsymbol{z}_{m,n}$ and $\boldsymbol{q}_{r,s}$ respectively. Vectors $\boldsymbol{x}_1, \boldsymbol{x}_2$ and $\boldsymbol{k}_1, \boldsymbol{k}_2$ are defined by mesh geometry, and not by the placement of discrete degrees of freedom.

For the distribution of energy over scales in eddy-resolving simulations, a commonly applied scale separation method relying on basis decomposition is Fourier analysis which separates the data into waves of different wavelengths. However, Fourier analysis relies on a set of assumptions that are not always met by model or observational data. Two of the most common discrepancies are the potential lack of regular, equidistant data points in case of unstructured data and the lack of periodicity along boundaries in case of complex domains. In this study, we will discuss some of the issues related to Fourier analysis in the context of a model with triangular rather than rectangular spatial discretization. We will also introduce and discuss the possibility of an alternative analysis that uses the Walsh–Rademacher basis (indicator functions) instead of the Fourier basis which, in many respects, is more suitable for unstructured data.

Observational data is often inherently unstructured due to the nature of local measurements. When it comes to numerical modeling, on the other hand, some models are also formulated on unstructured triangular meshes and place the degrees of freedom (DoF) on vertices or triangles. They include, for example, global-scale models such as FESOM (Danilov et al., 2017), ICON (Korn, 2017) and coastal models such as FVCOM (Chen et al., 2003), SCHISM (Zhang et al., 2016), or SUNTANS (Fringer et al., 2006). Concerning Fourier analysis, the first question that arises for such models is: Which wavenumbers can be represented on triangular meshes? Relying on well-known facts from solid-state physics (e.g., Kittel, 2004), one can link the representable wavenumbers to the notion of primitive translation vectors. They define a primitive mesh cell, a reciprocal lattice in wavenumber space, and the smallest resolved wavelengths (see illustration in Figure 1). On regular triangular meshes the primitive cell is a rhombus consisting of two triangles with opposite orientation. Importantly, the number of triangles is approximately twice that of the mesh vertices, which creates an illusion that the DoF placed on triangles resolve larger wavenumbers than the DoF placed at vertices. It turns out that the increased number of DoF leads to modes of variability inside of the unit cells of the respective grid (i.e., internal variability modes), leaving the representable wavenumbers without changes. Irregular triangular grids further complicate the definition of the highest resolved wavenumber and the spectral density. In this study, however, we will focus on the resolution of regular triangular grids, while the definition and theory for the resolution of irregular triangular grids will be left for future studies.

In order to compute classical Fourier spectra on general (unstructured) meshes, one cannot rely on a regular placement of the DoF and has to interpolate to a regular quadrilateral grid. This leads to some (arbitrary) sampling of original data, which generally does not create ambiguities for the spectra of variance which are rapidly decaying at large wavenumbers. However, larger uncertainties may occur for the power spectra of dissipation (due to horizontal viscosity or diffusion). Such spectra are needed, for example, to judge on the effective resolution, which is the smallest scale where dynamics are unaffected by (numerical) dissipation (Soufflet et al., 2016). They are also necessary to intercompare different types of momentum closures. The dissipation power on unstructured meshes is computed as a dot product between a field and its dissipation tendency which depends on the numerical operator that parameterizes the small scales in the momentum equation. The dissipation tendency is often noisy

and has a large grid scale contribution, generally because the commonly applied harmonic or biharmonic operators emphasize large wavenumbers. The placement of DoF on triangles may further emphasize the grid-scale variability because of the difference in the orientation of computational stencils for any two adjacent triangles. Interpolation can be further affected by this geometrical mode in the placement of triangle centers as illustrated in Figure 1. Computations are still possible, but require care. This study will both illustrate the difficulties in the computations as well as possible remedies. New alternative methods that avoid interpolation will be discussed and compared to the results of traditional Fourier analysis. They can be seen as an extension to already existing methods such as Aluie et al. (2018), Grooms et al. (2021) which mostly focus on scale analysis and scale separation for structured meshes and for scales considerably larger than the grid scale.

We ran into issues raised above in our earlier attempt to compute spectra of dissipation power for runs with different momentum closures. Classical, purely viscous closures such as the Smagorinsky (Smagorinsky, 1963) or Leith parametrizations (Leith, 1996) are designed to be entirely dissipative on all scales with an emphasis on small scale dissipation (see discussions in e.g., Bachman et al., 2017; Fox-Kemper & Menemenlis, 2008; Pearson et al., 2017). A variety of other approaches have emerged in recent years, among which are kinetic energy backscatter parameterizations (e.g., Jansen & Held, 2014; Jansen et al., 2015; Juricke, Danilov, Koldunov, Oliver, Sein, et al., 2020; Juricke, Danilov, Koldunov, Oliver, & Sidorenko, 2020; Juricke et al., 2019; Klöwer et al., 2018; Perezhogin, 2019). Contrary to purely viscous closures, energy backscatter parameterizations enable energy injection on large scales but dissipation on small scales. They still retain an overall dissipative nature when averaged across all scales. Scale analysis of dissipation power can highlight this scale dependence of momentum closures and is, therefore, an important diagnostic to investigate the behavior of momentum closures, especially close to the grid scale. However, as illustrated in this study, one can easily get a substantially distorted result if one is not careful. Practical illustrations of these issues rely on data obtained with FESOM2 (Danilov et al., 2017) for the zonally reentrant channel test case of Soufflet et al. (2016) which focuses on the simulation of mesoscale turbulence and was run with two different momentum closures, one purely dissipative parametrization (following Leith, 1996) and one kinematic backscatter (KBACK) parametrization (following Juricke, Danilov, Koldunov, Oliver, Sein, et al., 2020).

In this study, we caution against using interpolation methods for unstructured data without considering the properties of the underlying data and the respective interpolation method. We seek to develop new diagnostic methods that enable scale analysis under five specific constraints:

- The method needs to be applicable both to global (spherical) data as well as confined regions to allow a focus on specific local dynamics.
- The diagnostic should be able to deal with ocean data, that is, coastlines of continents and islands should not pose a fundamental problem and should not lead to substantial aliasing of the spectrum.
- Unstructured data will be difficult to assess in terms of the highest resolved wavenumber, but the diagnostic should be extendable to this kind of data with minimal impact and deterioration of the spectrum only for the highest wavenumbers.
- The diagnostic should not implicitly assume smoothness of the data if it is not supported by theory. In particular, scale analysis of dissipation power must not assume smoothness, so that we need a method that works well for both smooth (e.g., kinetic energy) as well as non-smooth fields.
- When the data comes from a model or source where it is treated in the finite volume sense, the diagnostics should respect this interpretation. In fact, this is the most we can assume when the data does not represent samples of a smooth field.

Some existing methods address some of these aspects. Tools such as SHTools (Wieczorek & Meschede, 2018) allow for spherical harmonic transforms that are specifically suited for global data on the sphere, but can also be applied to more or less arbitrary domain data via windowing. The routine SHExpandLSQ (https://shtools.github.io/SHTOOLS/pyshexpandlsq.html) also allows to use unstructured data by expanding irregularly spaced data into spherical harmonics using a least squares inversion. However, for confined local or complex domains spherical harmonics are not the ideal expansion. Even for spherical global ocean data, such methods need to deal with the complex topography of the oceans. As already mentioned for SHTools, this necessitates some form of windowing or padding of, for example, continents which may introduce additional errors. As a global analysis, the relation between wavenumber and wavelengths is also not straight forward for spherical harmonics when it comes to different regions around the globe, that is, same wavenumbers at the poles correspond to different wavelengths

than those in the tropics. A least squares inversion is a good approach for smooth data such as kinetic energy spectra, but introduces bias for non-smooth fields due to the fact that it treats the data as point-wise and reduces its variance, that is, smooths the data. We will address a similar issue regarding smooth interpolation methods in this study.

For local domains, 2D Fourier transforms may be more suited. However, they will have to deal with periodicity constraints at the boundaries and respective windowing. Furthermore, while nonuniform Fourier transforms exist, in practice for fast implementation they also necessitate some form of interpolation and oversampling (e.g., Ruiz-Antolín & Townsend, 2018) which tends to smooth discontinuous data. It is also generally necessary to avoid complex boundaries, so it is commonly applied to rectangular regions without islands or continents (e.g., Khatri et al., 2018). Finally, the aforementioned smoothing filter of for example, Aluie (2019) can potentially be applied to the global ocean (Storer et al., 2022), but one still needs to deal with complex boundaries via, for example, padding. Furthermore, extending these approaches to unstructured data is not straight forward.

The methods and issues we present here are focused on the aspect of local domains, regular triangular grids and their application to both smooth as well as non-smooth data. Extensions to fully irregular triangular grids and global spherical geometry with complex boundaries is conceptually possible, but will need further research. We will discuss such research perspectives in the last section. As a reference to compare our new methods with, we will use 2D Fourier spectra with interpolations to a rectangular grid as such spectra are commonly used and suitable for the limited domains discussed in this study.

This study is structured as follows. We begin with Fourier analysis in Section 2. We discuss which wavenumbers can be represented on triangular meshes and explain some of the consequences for the computation of spectra on interpolated regular grids. In Section 2.4, we provide a short description of an alternative approach, the resize-and-average (R-a-A) method, which does not rely on the Fourier basis, but on the Walsh–Rademacher basis instead. A third diagnostic based on the applications of smoothing filters is also introduced. Section 3 describes simulations with two different momentum closures, the Leith and KBACK parametrizations, for which we will assess kinetic energy and dissipation power spectra. The next Section 4 applies all three scale diagnostics to the aforementioned simulation data. The paper closes with discussions and conclusions in Section 5.

2. Spectra on Triangular Meshes

2.1. Resolved Wave Numbers for a Regular Triangular Mesh

Consider an infinite regular triangular mesh composed of equilateral triangles. We introduce coordinates $\boldsymbol{x} = (x, y)$ with origin at one of the mesh vertices and orient the triangles so that all vertices are obtained from (0,0) through the set of translations

$$\boldsymbol{z}_{m,n} = m\,\boldsymbol{x}_1 + n\,\boldsymbol{x}_2, \quad \boldsymbol{x}_1 = a\,(1,0), \quad \boldsymbol{x}_2 = a\,(1/2, \sqrt{3}/2), \tag{1}$$

where a is the triangle side length (see also Figure 1), and m, n are integers. The vectors $\boldsymbol{x}_1$ and $\boldsymbol{x}_2$ are referred to as primitive translation vectors. The mesh is invariant to translation by $\boldsymbol{z}_{m,n}$. A rhombus, defined by vectors $\boldsymbol{x}_1$ and $\boldsymbol{x}_2$, is a primitive unit cell of the triangular lattice. The selection of vectors $\boldsymbol{x}_1$ and $\boldsymbol{x}_2$ and the unit cell is not unique. For example, one can select $\boldsymbol{x}_1$ and $\boldsymbol{x}_2 - \boldsymbol{x}_1$, and take a rhombus that corresponds to them. However, all possibilities represent the same group of translations $\boldsymbol{z}_{m,n}$.

The values of a Fourier harmonic of any scalar or vector field $T = \overline{T}\,\mathrm{e}^{\mathrm{i}\boldsymbol{k}\cdot\boldsymbol{x}}$, with amplitude $\overline{T}$ and wave vector $\boldsymbol{k} = (k, l)$, sampled at vertices or centers of similarly oriented triangles do not change if $\boldsymbol{k}$ is replaced by $\boldsymbol{k} + \boldsymbol{q}$, where $\boldsymbol{q}$ is such that

$$\mathrm{e}^{\mathrm{i}\boldsymbol{q}\cdot\boldsymbol{z}} = 1. \tag{2}$$

This implies that

$$\boldsymbol{q} = \boldsymbol{q}_{r,s} = r\,\boldsymbol{k}_1 + s\,\boldsymbol{k}_2, \tag{3}$$

where r and s are integers and the vectors $\boldsymbol{k}_1$ and $\boldsymbol{k}_2$ are such that

$$\boldsymbol{x}_i \cdot \boldsymbol{k}_j = 2\pi\,\delta_{ij}, \tag{4}$$

which gives

$$\boldsymbol{k}_1 = 2\pi/a\,(1, -1/\sqrt{3}), \quad \boldsymbol{k}_2 = 2\pi/a\,(0, 2/\sqrt{3}). \tag{5}$$

The translations $\boldsymbol{q}_{r,s}$ define the reciprocal lattice in $\boldsymbol{k}$-space (Figure 1).

Because $\boldsymbol{k}$ can be determined up to the translation $\boldsymbol{q}_{r,s}$, it is sufficient to consider only $\boldsymbol{k}$-points that are closer to the origin $\boldsymbol{q}_{0,0}$ than to any other $\boldsymbol{q}_{r,s}$. These points lie in the Voronoi polygon obtained by the Voronoi tesselation of the lattice $\{\boldsymbol{q}_{r,s}\}$ in $\boldsymbol{k}$-space. This hexagon is referred to as the first Brillouin zone and is shown in Figure 1.

The reciprocal lattice and the Brillouin zone are defined by the geometry of the triangular mesh and do not depend on how discrete DoF are placed, unless the DoF and discretization correspond to a refinement of the given triangular mesh. As a result, one deals with $\boldsymbol{k}$ constrained to the first Brillouin zone independent of whether the discrete DoF are placed on vertices or cells or edges.

The smallest distance from $\boldsymbol{q}_{0,0}$ to the boundary of the first Brillouin zone is

$$|\boldsymbol{k}|_{\max} = 2\pi/(\sqrt{3}a) = \pi/h,$$

that is, the *geometric* resolution of the equilateral triangular mesh is defined by the height of triangles h. This can be compared with $|\boldsymbol{k}|_{\max} = \pi/a$ for the quadrilateral mesh with the side a.

On triangular meshes there are nearly twice as many cells as vertices. If discrete DoF are placed on cells, an obvious question is how the increased number of DoF can be reconciled with the statement that the wave vector is constrained in the same way to the first Brillouin zone as for the vertex placement. The answer is that the increased number of DoF in this or similar cases creates additional modes of variability inside the unit cells, as explained, for example, in Danilov and Kutsenko (2019). The origin of the mode is related to the difference in the orientation of the stencil of the nearest neighbors. For a triangle pointing upward in the plane of Figure 1 the stencil of three nearest neighbors points downward, and vice versa. Consequently, discrete operators have different representation on u (upward pointing) and d (downward pointing) triangles, and different truncation errors, hence a mode of variability between the nearest triangles. As a rule, this mode of variability is well controlled in the existing numerical codes (see, e.g., the discussion of viscous operators in Juricke, Danilov, Koldunov, Oliver, Sein, et al. (2020) for FESOM), but can contribute to the apparent grid-scale patterns seen in the dissipation tendency (see Section 4.1.2).

2.2. Fourier Spectra of Interpolated Fields

Triangular meshes used in practice are generally non-uniform. The most common way to compute spectra in this situation is to interpolate the fields onto a regular quadrilateral mesh, then sample and apply the discrete Fourier transform in the standard way. The theoretical consideration above gives an argument on the resolution of the sampling mesh (finer than $\pi/k_{\max}$). Due to interpolation, some variance can be lost on small scales.

Consider, for definiteness, a scalar discrete field ϕ_c known on mesh cells. When computing spectra of vector fields, such as kinetic energy spectra, the expressions stated here apply component-wise in the respective dot products. We write $c \in \mathcal{T}$ to denote the cell index and $\mathcal{T}$ to denote the set of mesh triangles. If ϕ_{mn} is the result of interpolation of the cell-based ϕ_c to some regular grid, with $1 \le m \le M$ and $1 \le n \le N$, covering the domain of interest, to compute the power spectrum of ϕ, one needs to ensure variance preservation in the sense

$$\frac{1}{MN}\sum_{m,n=1}^{M,N} \phi_{mn}^2 \approx \frac{\sum_{c\in\mathcal{T}} \phi_c^2\,|A_c|}{\sum_{c\in\mathcal{T}} |A_c|} \tag{6}$$

(for simplicity, we assume that the respective field ϕ has zero mean when averaged over the entire domain or all frequencies). Here, $|A_c|$ denotes the area of cell c.

This is easy to achieve if ϕ_c is a primitive variable (velocity, temperature or salinity) with commonly available linear or cubic spline interpolation because such fields are commonly smooth. They are generally known in a finite-volume sense as mean over the respective control volumes. The nearest point interpolation method to a

sufficiently fine mesh tends to respect this sense, yet emphasizes discontinuities in interpolated data, which leads to an artificial spectral pile-up at small scales. Linear and cubic interpolation methods are free from such a drawback, but treat the finite-volume data as point values. Although this is appropriate for smooth fields, it leads to artifacts in the case of spectra of horizontal dissipation power as discussed later.

To compute dissipation power spectra, one has to interpolate both ϕ_c and the dissipation tendency, which is either due to the horizontal diffusion or horizontal viscosity, apply the Fourier transform to both, and compute their inner product. The dissipation tendency on cells will be written as $(\mathsf{L}\phi)_c$, where L is a discrete Laplacian operator in the simplest case, but can be a more complicated operator for more sophisticated viscous or backscatter closures if these are applied in a given simulation. On regular meshes, one can use a discrete analog of the divergence theorem in the form

$$\int_\Omega \phi\,\Delta\phi\,\mathrm{d}V = -\int_\Omega |\nabla\phi|^2\,\mathrm{d}V + \int_{\partial\Omega} \phi\,\boldsymbol{n}\cdot\nabla\phi\,\mathrm{d}S, \tag{7}$$

where the second integral is over the boundary $\partial\Omega$ of the integration domain Ω and is negligible if the domain is large enough, as averaged boundary fluxes for sufficiently smooth fields tend to zero for sufficiently large areas. If the boundary conditions for the entire domain are posed in a no-flux form this statement holds exactly, but it generally also holds in an approximate sense for sufficiently large areas smaller than the total domain. As a result, one can compute a power spectrum of $\nabla\phi$ instead of computing the cross-spectrum. While discrete analogs of similar transformations are maintained on unstructured meshes, they are not always straightforward (see Juricke et al., 2019, for FESOM operators), and may be not available in model output.

In applications, the field ϕ_c is generally smooth while $(\mathsf{L}\phi)_c$ often has a noticeable grid-scale component. Indeed, if the power spectrum of ϕ scales as $k^{-\alpha}$, the envelope of the Fourier transformed $\phi_{\boldsymbol{k}}$ scales as $k^{-(\alpha+1)/2}$. The dissipation tendency scales as $k^{-(\alpha+1)/2+2}$ for the harmonic operator L and as $k^{-(\alpha+1)/2+4}$ for the biharmonic one. Thus, when $\alpha = 3$, the envelope of the Fourier transform of the dissipation tendency is flat even for a harmonic operator. This amplification of small scales is common to all discretizations, and explains why the pattern of $\mathsf{L}\phi$ can look noisy. For cell-based quantities on triangular meshes there is one more factor, namely the difference of L on u and d triangles. Here, the internal degree of freedom is another source of small-scale noise not present in the case of vertex-based quantities on triangular meshes or in the case of cell-based quantities on quadrilateral meshes.

Because of the grid-scale pattern, even oversampling may fail to ensure that $\mathsf{L}\phi$ is properly sampled. Writing $(\mathsf{L}\phi)_{mn}$ to denote the interpolation of the cell-based quantity $(\mathsf{L}\phi)_c$ to the sampling grid, we need to achieve

$$\frac{1}{MN}\sum_{m,n}^{M,N} \phi_{mn}\,(\mathsf{L}\phi)_{mn} \approx \frac{\sum_{c\in\mathcal{T}} \phi_c\,(\mathsf{L}\phi)_c\,|A_c|}{\sum_{c\in\mathcal{T}} |A_c|}. \tag{8}$$

This approximation is prone to fail, depending on the method of interpolation. For FESOM2, we will show in Section 4.1.2 that scale analysis of kinetic energy dissipation is very sensitive to the specific choice of interpolation onto a regular grid, especially for simulations that use the backscatter parameterization (Juricke, Danilov, Koldunov, Oliver, Sein, et al., 2020). For those simulations, dissipation spectral density is negative in the vicinity of $k_{\max}$, but can be positive at smaller wavenumbers. The total dissipation power is negative, but this picture is easily distorted through interpolation. The accuracy in representing the dissipation power by the interpolated field (such that Equation 8 approximately holds) may serve as a check for the appropriateness of interpolation. Furthermore, angular averaging of two-dimensional spectra, collapsing them to one-dimensional spectra helps to reduce the side effects of interpolation errors.

2.3. On 1D Spectra

1D spectra are a convenient characteristic in test cases that use periodic boundary conditions in one direction (e.g., zonally reentrant channels). Data are taken along zonal lines, and no windowing is needed. The spectra computed at different meridional locations are then averaged. On regular equilateral triangular meshes such lines are drawn through centroids of u or d triangles. Since the distance between the nearest data point is a, not all wavenumbers are resolved (π/a instead of π/h). Taking data points along a zigzag line passing through centroids of u and d triangles is potentially resolving higher wavenumbers, but may create aliasing. If one interpolates to a regular set of points along a zonal line, the result will depend on the line (and interpolation method). If the line is

drawn through the centers of triangles, only the data at these centers will be used for linear interpolation. Spectral density at wavenumbers larger than π/a will still be uncertain.

There is a simple, fundamental reason why especially one-dimensional spectra of dissipation are questionable: In the continuous 2D case for $\mathsf{L} = \Delta$,

$$\phi\,\Delta\phi = \boldsymbol{\nabla}\cdot(\phi\,\boldsymbol{\nabla}\phi) - |\boldsymbol{\nabla}\phi|^2, \tag{9}$$

so that the first (flux divergence) term on the right-hand side does not contribute to 2D spectra (being the divergence of the product), leading to a negative-definite spectral density. However, it will always contribute to 1D spectra of dissipation, and may even give a dominant contribution. Averaging of 1D spectra over the other direction will not necessarily fully eliminate this contribution, leading to an unpredictable result.

In our experience, meridionally averaged 1D spectra are highly sensitive to the choice of interpolation method and the location of the interpolation grid, especially for dissipation power spectra which are relatively flat. We found that interpolation such as linear or cubic may actually lead to considerably distorted line structures on the interpolated grid, depending on the orientation of the triangles. Consequently, the result for cubic and linear interpolation and zonal 1D dissipation power spectra turns out to be fundamentally wrong (not shown), as the linear and cubic interpolations smooth out the small scales and project them onto much large scales in the zonal direction. Even by averaging in the meridional direction, this error is not alleviated and, instead, we produce spectra that show substantially distorted dissipation powers on large scales. Kinetic energy spectra, on the other hand, are not much affected by this due to the rapidly decaying high wavenumber contribution and can also be computed using 1D spectra averaged in the meridional direction. While we will not discuss one-dimensional line spectra any further, we would like to highlight that these details and consequences need to be kept in mind when considering 1D spectra on interpolated meshes.

2.4. Scale Analysis Based on Characteristic Functions

In this section and Section 2.5, we present two alternative approaches to scale analysis that avoid interpolation and preserve the finite-volume sense in which the data is represented in the model. The first method is called resize-and-average method (R-a-A) and we will present it in its original and a modified version. In the following, we describe the general concept relying on averaging operators on successively smaller subdomains of the model domain using the Walsh–Rademacher basis, that is, a basis generated by indicator functions of cells of the triangular grid. A detailed mathematical analysis of this method and a comparison of Fourier spectra and Walsh–Rademacher spectra for random fields with a power-law rate of spectral decay can be found in A. Kutsenko et al. (2022). This paper also describes the limitations of R-a-A and discusses strategies for overcoming these limitations.

We identify the data on cells, ϕ_c, with the piecewise-constant function

$$\phi(\boldsymbol{x}) = \sum_{c\in\mathcal{T}} \phi_c\,\chi_{A_c}(\boldsymbol{x}), \tag{10}$$

where $\chi_{A_c}(\boldsymbol{x})$ is the indicator function of mesh cell A_c, so that $\phi(\boldsymbol{x}) = \phi_c$ for $\boldsymbol{x}$ within A_c. Generally, the A_c may be triangles or unions of triangles.

Now consider a submesh $\mathcal{S}$ with elements B_c composed of unions of several neighboring A_c, that is,

$$B_c = \bigcup_{c'\in\mathcal{T}_c} A_{c'} \tag{11}$$

for $c \in \mathcal{S}$, where $\mathcal{T} = \cup_{c\in\mathcal{S}}\mathcal{T}_c$ is a partition of the initial mesh. The initial mesh $\mathcal{T}$ generates the Hilbert space

$$L_{\mathcal{T}} = \operatorname{span}\left\{\chi_{A_c} : c \in \mathcal{T}\right\}. \tag{12}$$

The coarser sub-mesh generates the Hilbert subspace

$$L_{\mathcal{S}} = \operatorname{span}\left\{\chi_{B_c} : c \in \mathcal{S}\right\}. \tag{13}$$

The orthogonal projector onto $L_{\mathcal{S}}$ is given by

$$(\mathbb{P}_S\phi)(\boldsymbol{x}) = \sum_{c\in S} |B_c|^{-1} \left(\sum_{c'\in\mathcal{T}_c} \phi_{c'} \, |A_{c'}| \right) \chi_{B_c}(\boldsymbol{x}). \tag{14}$$

This gives a decomposition, orthogonal with respect to the standard L^2-inner product

$$\langle \phi, \psi \rangle = \int \phi(\boldsymbol{x})\, \psi(\boldsymbol{x})\, \mathrm{d}\boldsymbol{x}, \tag{15}$$

of the space $L_\mathcal{T}$ into the coarse subspace L_S with a remainder denoted by $L_{\mathcal{T}/S}$

$$L_\mathcal{T} = L_S \oplus L_{\mathcal{T}/S}. \tag{16}$$

A field ϕ then decomposes into the orthogonal sum

$$\phi = \mathbb{P}_\mathcal{T}\phi = \mathbb{P}_S\phi + \mathbb{P}_{\mathcal{T}/S}\phi, \tag{17}$$

so that

$$\langle \phi, \psi \rangle = \langle \mathbb{P}_\mathcal{T}\phi, \mathbb{P}_\mathcal{T}\psi \rangle + \langle \mathbb{P}_{\mathcal{T}/S}\phi, \mathbb{P}_{\mathcal{T}/S}\psi \rangle, \tag{18}$$

where the contribution of the remainder subspace is given by

$$\begin{aligned} \langle \mathbb{P}_{\mathcal{T}/S}\phi, \mathbb{P}_{\mathcal{T}/S}\psi \rangle &= \langle \phi, \psi \rangle - \langle \mathbb{P}_\mathcal{T}\phi, \mathbb{P}_\mathcal{T}\psi \rangle \\ &= \sum_{c\in\mathcal{T}} \phi_c\, \psi_c\, |A_c| - \sum_{c\in S} |B_c|^{-1} \left(\sum_{c'\in\mathcal{T}_c} \phi_{c'}\, |A_{c'}| \right) \left(\sum_{c'\in\mathcal{T}_c} \psi_{c'}\, |A_{c'}| \right). \end{aligned} \tag{19}$$

Through subsequent coarsening, we can construct a hierarchy of subspaces, with the original mesh $\mathcal{T}$ at the small-scale end going to larger and larger scales.

To compute a spectrum using this construction, we proceed as follows. Consider a sufficiently large square box B^1 with side length L, covering some part of the computational mesh. L is generally chosen to be sufficiently large to create a square box that covers most of the area of interest. As the coarsest mesh, denoted $\mathcal{T}^1$, we take the union of those triangles from $\mathcal{T}$ whose centroids lie inside B^1. Now introduce a sequence of child bounding boxes obtained by splitting the box B^1 into equal-sized smaller boxes. The smaller boxes will be denoted as $B^n_{\boldsymbol{m}}$, where the index n indicates that the length of the side of the respective box is L/n, and $\boldsymbol{m}$ is the shortcut for a pair of indices $\boldsymbol{m} = (m_x, m_y)$, $1 \le m_x, m_y \le n$, describing the position of $B^n_{\boldsymbol{m}}$ within B^1. For each child box, we look for a subset $\mathcal{T}^n_{\boldsymbol{m}}$ of $\mathcal{T}^1$ including the indices of triangles with centers within $B^n_{\boldsymbol{m}}$. For every fixed n, $\{\mathcal{T}^n_{\boldsymbol{m}}\}$ is a partition of $\mathcal{T}^1$, and we set

$$\mathcal{T}^n = \bigcup_{\boldsymbol{m}} \mathcal{T}^n_{\boldsymbol{m}}. \tag{20}$$

We stop at $n = N$ such that all $\mathcal{T}^n_{\boldsymbol{m}}$ include not more than one triangle. Subsequent refinement will be excessive.

When n_1 is a divisor of n_2, the subspaces associated with $\mathcal{T}^{n_1}$ and $\mathcal{T}^{n_2}$ are orthogonal so that the norm of the projection to $L_{\mathcal{T}^{n_2}/\mathcal{T}^{n_1}}$ is a measure of the contribution from the scale range $[L/n_1, L/n_2)$ to the total energy.

There is some arbitrariness in this construction as the areas occupied by triangles belonging to different $\mathcal{T}^n_{\boldsymbol{m}}$ are not equal. The relative differences will be small when n is small, but may be large for $n \approx N$. It is possible to get an estimate on the resulting uncertainty by slightly displacing the box B^1 and repeating computations. The advantage of this method is that it works for structured as well as unstructured meshes.

Here, to obtain a finer separation at smaller scales, we chose $n_1 = n$ and $n_2 = n + 1$, define the scale points

$$\ell_n = \frac{L}{n}, \tag{21}$$

the spectral energy density

$$E(\ell_n) = \langle \mathbb{P}_{\mathcal{T}^n} u - \mathbb{P}_{\mathcal{T}^{n+1}} u, \mathbb{P}_{\mathcal{T}^n} u - \mathbb{P}_{\mathcal{T}^{n+1}} u \rangle, \tag{22}$$

and the spectral dissipation power density

$$E_{\mathrm{dis}}(\ell_n) = \langle \mathbb{P}_{\mathcal{T}^n} u - \mathbb{P}_{\mathcal{T}^{n+1}} u, \mathbb{P}_{\mathcal{T}^n} \mathsf{L} u - \mathbb{P}_{\mathcal{T}^{n+1}} \mathsf{L} u \rangle. \tag{23}$$

The dissipation tendency is given by $\mathsf{L}u$ and depends on the velocity field u and the momentum closure represented by the operator L. Figure 8 shows examples of an energy spectrum (ℓ_n, $E(\ell_n)$), left, and a dissipation power spectrum (ℓ_n, $E_{\mathrm{dis}}(\ell_n)$), right.

In the orthogonal case, when n_1 divides n_2,

$$\langle \mathbb{P}_{\mathcal{T}^{n_2}} u - \mathbb{P}_{\mathcal{T}^{n_1}} u, \mathbb{P}_{\mathcal{T}^{n_2}} u - \mathbb{P}_{\mathcal{T}^{n_1}} u \rangle = \langle \mathbb{P}_{\mathcal{T}^{n_2}} u, \mathbb{P}_{\mathcal{T}^{n_2}} u \rangle - \langle \mathbb{P}_{\mathcal{T}^{n_1}} u, \mathbb{P}_{\mathcal{T}^{n_1}} u \rangle, \tag{24}$$

and

$$\langle \mathbb{P}_{\mathcal{T}^{n_2}} u - \mathbb{P}_{\mathcal{T}^{n_1}} u, \mathbb{P}_{\mathcal{T}^{n_2}} \mathsf{L} u - \mathbb{P}_{\mathcal{T}^{n_1}} \mathsf{L} u \rangle = \langle \mathbb{P}_{\mathcal{T}^{n_2}} u, \mathbb{P}_{\mathcal{T}^{n_2}} \mathsf{L} u \rangle - \langle \mathbb{P}_{\mathcal{T}^{n_1}} u, \mathbb{P}_{\mathcal{T}^{n_1}} \mathsf{L} u \rangle. \tag{25}$$

When $n_1 = n$ and $n_2 = n{+}1$ and these identities no longer hold, experiments show that the left-hand expressions in Equations 24 and 25 are less noisy than the respective right-hand expression, which motivates their choice for the diagnostics (22) and (23). A theoretical justification for this choice and a mathematical analysis along the lines of A. Kutsenko et al. (2022) of this modified extended version of the R-a-A method is open and a topic of current research.

The practical implementation of the modified R-a-A method used in the remainder of this paper was done as follows.

1. We organize the velocity data as a 2D array, that is, as a matrix $\mathbf{U}$. The most accurate way to do this is by computation of the area of intersection between the irregular grid and a regular square or rectangular grid, that is, by projecting the irregular grid onto the regular grid. However, any organization of irregular data into the matrix which satisfies the condition that (almost) neighboring cells in the matrix correspond to (almost) neighboring points or elements in the irregular grid will still give relevant results. Of course, the accuracy of such approximation should be based on synthetic tests done for known fields. Now, the whole matrix $\mathbf{U}$ corresponds to the resolutions $[0, L]$, that is, from scale 0 to scale L (For convenience, we use scales instead of wavenumbers which are proportional to 1/scales.)
2. We divide $\mathbf{U}$ into $m \times m$ sub-matrices $\mathbf{U}_{ij}$ with equal sizes and then replace each of these sub-matrices by the constant submatrix $\tilde{\mathbf{U}}_{ij}$ where all cells contain the average value of $\mathbf{U}_{ij}$:

$$\mathbf{U} = \begin{pmatrix} \mathbf{U}_{11} & \cdots & \mathbf{U}_{1m} \\ \vdots & & \vdots \\ \mathbf{U}_{m1} & \cdots & \mathbf{U}_{mm} \end{pmatrix} \rightarrow \mathbf{U}_m = \begin{pmatrix} \tilde{\mathbf{U}}_{11} & \cdots & \tilde{\mathbf{U}}_{1m} \\ \vdots & & \vdots \\ \tilde{\mathbf{U}}_{m1} & \cdots & \tilde{\mathbf{U}}_{mm} \end{pmatrix}.$$

   The resulting matrix, $\mathbf{U}_m$, is the projection of $\mathbf{U}$ onto the scales $[L/m, L]$. The norm $\|\mathbf{U}_m - \mathbf{U}_{m+1}\|^2 = \langle \mathbf{U}_m - \mathbf{U}_{m+1}, \mathbf{U}_m - \mathbf{U}_{m+1} \rangle$ gives the energy corresponding to the scales $[L/(m{+}1), L/m]$, see Equation 22. The corresponding dissipation energy is $\langle \mathbf{U}_m - \mathbf{U}_{m+1}, \mathbf{D}_m - \mathbf{D}_{m+1} \rangle$, where $\mathbf{D}$ contains the corresponding values of $\mathsf{L}u$, see Equation 23.
3. The matrices we compare, $\mathbf{U}_m$ and $\mathbf{U}_{m+1}$, should have the same size. We can achieve this by doubling, tripling, etc., the values in the initial matrix $\mathbf{U}$. Indeed, let us assume a square mesh for simplicity. Then the matrices

$$\begin{pmatrix} a & b \\ c & d \end{pmatrix}, \quad \begin{pmatrix} a & a & b & b \\ a & a & b & b \\ c & c & d & d \\ c & c & d & d \end{pmatrix}$$

describe the same field if we assume that both correspond to the same scales and that both matrices represent a piece-wise constant field. This assumption is natural in the context of the R-a-A method since Walsh–Rademacher basis functions are piece-wise constant functions. Note that for the triangular meshes the procedure

of duplication, triplication, etc., is more complex. The explicit code for the original and the modified R-a-A methods is available at https://doi.org/10.5281/zenodo.7270043 (A. A. Kutsenko, 2022).

The method can be easily adapted to non-square (rectangular) initial matrices **U**., and we expect that it can be further extended to unstructured grids by computing the intersections of such grids with structured square grids for which the current modified R-a-A already works well.

2.5. Scale Analysis via Discrete Spatial Filtering

The second method, which is in some respect related to the R-a-A method, is based on the use of spatial filters. It also has conceptual overlap with, for example, Sadek and Aluie (2018), Grooms et al. (2021), but differs in the fact that it uses the natural discrete filter operation used in FESOM2.

More specifically, we apply several cycles of a smoothing filter that was also used by Juricke et al. (2019) and Juricke, Danilov, Koldunov, Oliver, Sein, et al. (2020) to enhance the spatial scale of the backscatter term of their backscatter parametrization. It projects via an area weighted average the field under consideration a_c, which is stored on cell centroids, first from the cell centroids to the vertices using the operator X

$$(\mathsf{X}a)_v = \sum_{c\in C(v)} a_c\,(|A_c|/3)/\sum_{c\in C(v)}(|A_c|/3), \tag{26}$$

where $C(v)$ is the set of cells containing vertex v. After that, the new quantity b_v defined on vertices is then averaged back to the centroids using the operator C

$$(\mathsf{C}b)_c = \frac{1}{3}\sum_{v\in\mathcal{V}(c)} b_v, \tag{27}$$

where $\mathcal{V}(c)$ is the set of vertices of cell c (see Juricke, Danilov, Koldunov, Oliver, Sein, et al., 2020, for more details). In this way, nearest neighbor averaging enhances the scale of the fields and filters out smaller scales. However, while the combined smoothing filter $\mathsf{F} = \mathsf{CX}$ is the same as the one used in the computational design of the viscous closure and it conserves globally integrated quantities, the smoothed fields are not orthogonal to each other, that is, larger scales are consecutively mixed with each iteration of the filter. Nevertheless, when one is specifically interested in the grid scale behavior and differences therein between different momentum closures, this method is quite useful when only few iterations are applied, as it focuses first on the smallest resolved scales. Furthermore, it allows to investigate the spatial structure of dissipation power for a single time instance, rather than relying on spatial and temporal averaging as is the case for Fourier analysis. This method was already used by Juricke, Danilov, Koldunov, Oliver, Sein, et al. (2020, their Figures 4 and 5) and we add this diagnostic here for completeness.

3. Data Setup

We use data generated by the ocean model FESOM2 in a channel setup described in Soufflet et al. (2016) with periodic boundaries in the east-west direction and fixed boundaries in the North and South. The domain has a zonal length of 500 km and a meridional length of 2,000 km. The grid spacing, that is, the edge length a of a triangular cell, is 20 km. Despite the ability of FESOM2 to locally refine the grid, we employ a regular triangular grid in this study (see Figure 1) as it corresponds to the idealized setup also used by Juricke, Danilov, Koldunov, Oliver, Sein, et al. (2020).

Following the discussion in Section 2, the smallest resolved wavelengths corresponding to wavenumbers π/h and π/a for a maximum channel length of $\sqrt{(500^2 + 2000^2)}$ are approximately 34.64 and 40 km. However, the highest wavenumber that can be ideally represented is along a zigzag line in the zonal direction between meridionally slightly shifted centroids (see Figure 1). In that case, the controids are in zonal direction only $a/2$ apart and the corresponding maximum wavenumber and minimal wavelength are $2\pi/a$ and 20 km, respectively. However, as mentioned in Section 2, part of the information for these higher wavenumbers beyond π/h and up to $2\pi/a$ may already be a reflection of the spectrum from second and higher Brillouin zones and may be part of the internal mode of variability inside the unit cell, that is, inside a rhombus consisting of two triangles of opposite orientation. We nevertheless plot the Fourier spectra up to these high wavenumbers in Section 4.1 to discuss the behavior at the grid scale.

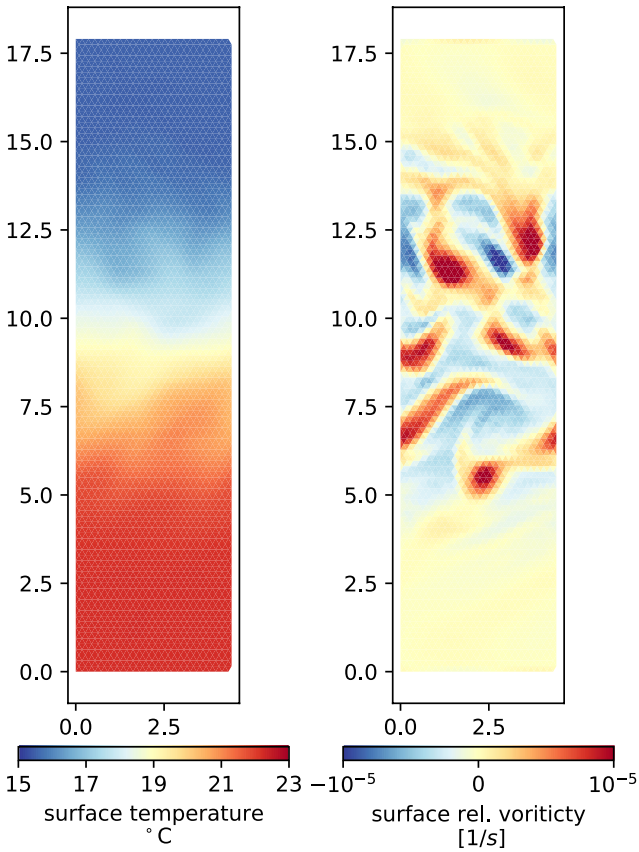

Figure 2. A daily mean of surface (left) temperature (°C) and (right) relative vorticity (1/s) from the Leith viscosity closure simulation at 20 km resolution, illustrating the eastward flow and enhanced turbulence in the center of the channel.

In the channel simulations, a South-North temperature gradient is reinforced through relaxation of the mean density profile, with warm temperatures in the South and cooler temperatures in the North. A mean current runs from West to East and mesoscale turbulence develops in the middle of the channel (see Figure 2). Simulations with different viscosity closures are available, using classical viscous closures such as Leith (1996), as well as recently developed backscatter closures, following, for example, the KBACK of Juricke, Danilov, Koldunov, Oliver, Sein, et al. (2020). In this study, we will focus on these two simulations, that is, one with a Leith viscosity closure (LEITH) and one with KBACK. The data was generated in the context of the recent study by Juricke, Danilov, Koldunov, Oliver, Sein, et al. (2020) where a KBACK parametrization was introduced—see the detailed discussion therein. We chose these two simulations as they are expected to behave fundamentally different when it comes to dissipation power spectra. While LEITH is purely dissipative on all scales (when taking into account the entire simulation domain), KBACK is expected to anti-dissipate on large scales and dissipate on small scales. Averaged over all scales, it is still dissipative. As we intend to investigate the detailed differences in dissipation behavior of various momentum closures in future studies, these two simulations serve as a testbed to assess the merits of the different scale analysis methods.

Given the data on the triangular grid, we employ several interpolation methods before computing classical 2D energy spectra. The interpolation methods between the triangular and the rectangular mesh vary in both the chosen interpolation scheme (nearest neighbor, linear, cubic) and the resolution of the interpolated grid ($0.09° = 10$ km, $0.045° = 5$ km, $0.01° \approx 1.1$ km). While a large variety of alternative interpolation methods are available, the three chosen schemes are widely used and cover different degrees of smoothness of the resulting estimate which is of fundamental relevance in this study. We compare smooth interpolation with different degrees of differentiability (linear and cubic) with discontinuous interpolation (nearest neighbor). Further details of the consequences of the interpolation scheme and the resolution of the interpolated grid will be discussed in the results section below.

The final spectra are always computed as an average of daily spectra for 9 years of simulation after the initialization year, that is, we neglect the first year after initialization from the mean state as the turbulence needs time to develop. To initiate the development of turbulence, a small perturbation is applied to the originally balanced mean state. Furthermore, in the spectra discussed below, we only show results for wavenumbers up to the grid resolution of $a = 20$ km. As we substantially oversample in the case of the interpolation grids with higher resolution, for example, at $0.01° \approx 1.1$ km, the highest wavenumbers above a wavelength of the nominal grid resolution of $2h \approx 34.64$ km partly correspond to a reflection of the spectrum. They contain some of the information from the resolved spectrum due to the reflection as well as the effects of the interpolation method. However, the even higher wavenumber part of the spectrum (which corresponds to oversampling of the interpolated grid) especially for lower wavelengths than $a = 20$ km does generally not contribute much and is therefore not considered further.

4. Results

4.1. Fourier Scale Analysis

We investigate the properties of Fourier spectral analysis obtained via equidistant sampling of interpolated data. Interpolation is done via nearest-neighbor, linear spline interpolation, or cubic spline interpolation. Sampling rates range from 2 times the triangular grid resolution $a = 20$ km (i.e., 10 km) to 18 times the grid scale (i.e., around 1.1 km). Even though the data is not strictly periodic in the meridional direction, turbulence is mostly restricted to the center of the channel and velocities are close to zero near the northern and southern boundaries. We verified that the use of a Hanning window to periodize the data did not change the results; all results shown are computed without windowing.

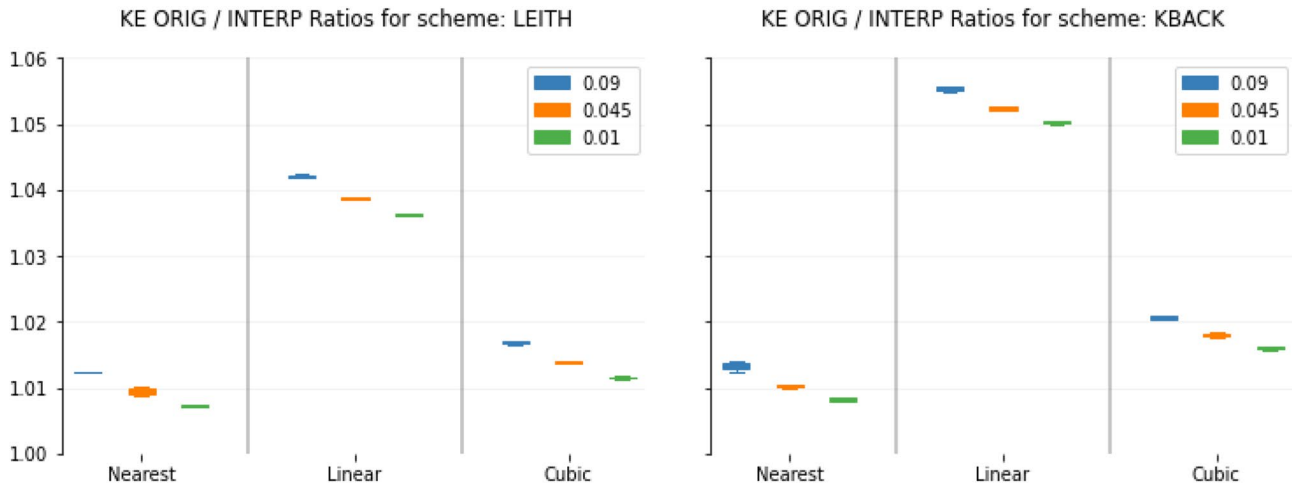

Figure 3. Ratio of average KE averaged for 1 year on original triangular versus interpolated grid for (left) the Leith viscosity closure simulation and (right) the kinematic backscatter simulation and various interpolation methods and interpolation grid resolutions. The boxes extend from the lower to upper quartile values generated by 9 interpolations with different origins to assess the sensitivity to the horizontal starting point of the interpolation. The upper whiskers end below Q3 + 1.5(Q3 − Q1) and the lower whiskers end above Q1 − 1.5(Q3 − Q1) with Q3 and Q1 the third and first quartile.

Spectra are shown as a function of inverse wavelength, obtained by summation over a wave number shell of width one in integer wavenumbers.

4.1.1. Kinetic Energy Spectra

As a first sanity check to assess the accuracy of the interpolation with respect to the area-averaged kinetic energy, we compute the ratio between the right and left-hand side of Equation 6, that is, the ratio of total kinetic energy on the original versus the interpolated grid. Deviations from 1 correspond to an error in total area-averaged kinetic energy through interpolation.

We find that the ratio is close to one in all cases (Figure 3). It is largely independent of the sampling ratio and only weakly dependent on the method of interpolation, with nearest-neighbor doing best, and linear interpolation the worst with a maximum error of around 5.5%. Furthermore, the method seems to be more or less independent from the choice of simulation, that is, whether we compute KE spectra for LEITH or KBACK, with slightly larger values and therefore differences for KBACK (about +0.01, i.e., +1%). Finally, slightly varying offsets of the original starting point for the interpolation (as illustrated by the boxes and whiskers in Figure 3) only lead to a noticeable variance in the ratios for the lowest resolution interpolation (i.e., 0.09° = 10 km).

Thus, on this measure, all methods are qualitatively suitable, even though quantitative differences already emerge. Whether the deviations from ratio 1 are acceptable is difficult to say, as the judgment also depends on the scales on which the differences eventually occur. If only the smallest scales are affected, moderate deviations may still be reasonable for kinetic energy as the small scales close to the grid scale in a model simulation are least reliable when it comes to their physical realism.

To further assess this question, we turn to actual spectra, choosing the highest oversampling ratio to be on the safe side for representing grid-scale features. First, we observe that the spectrum for LEITH has overall less KE on all scales when compared to KBACK (Figure 4). This is in line with the discussion of Juricke, Danilov, Koldunov, Oliver, Sein, et al. (2020) who developed kinetic energy backscatter for precisely the reason to reduce overdissipation and loss of KE in the KBACK simulation. This leads to a lift of kinetic energy levels especially for small wavenumbers by kinetic energy injection at scales sufficiently removed from the grid scale.

The choice of interpolation methods does not affect the large scales, but leads to substantial differences near the grid scale. This can be explained by the spectral slope of KE in our simulations, with expected power laws of slope between −5/3 and −3. Thus, an interpolation that acts discontinuously on the data, like nearest-neighbor interpolation, creates spurious contribution to the energy near the grid scale even though it remains closest to the finite-volume interpretation of the data. Continuous or smooth interpolation, on the other hand, will not change scaling laws near the grid scale. Consequently, linear or cubic interpolation retain the smoothness of the field

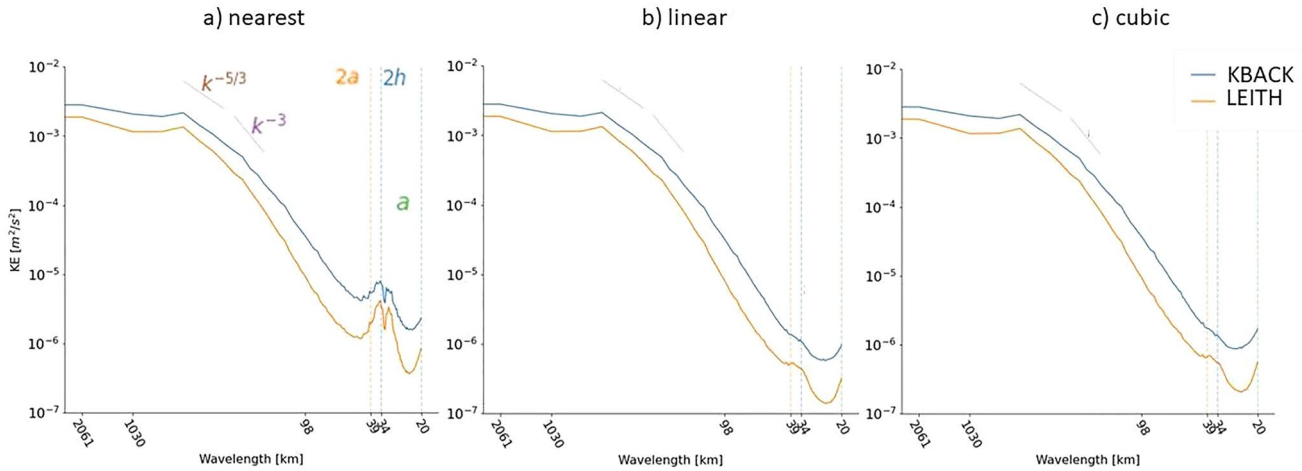

Figure 4. Kinetic energy spectra for simulations with Leith (orange) and kinematic backscatter (blue) momentum closures for (a) nearest neighbor, (b) linear and (c) cubic interpolated data to a 1.1 km grid, averaged for 9 years of simulation.

while still staying close—in an area averaged sense—to the original data. We conclude that especially cubic interpolation is here a sensible choice, as it provides a smooth high wavenumber spectrum as well as a close ratio representation between energy on the original and interpolated grid (see Figure 3).

Even though the choice of interpolation method is not critical for KE spectra, it will be crucial for quantities that have steeper or more shallow spectral slope. The shallow case is the main concern in this paper, and is discussed in detail in Section 4.1.2. On the other hand, when computing spectra of quantities that have less variation associated with high wavenumbers, the choice of a smooth interpolation method will be crucial. For example, the spectral slope of sea surface height is, according to theory, between $(-5/3) - 2 = -11/3$ and $-3 - 2 = -5$ (e.g., Wang et al., 2019). Any roughening of the high wavenumber part of the flow due to the interpolation can show up as a strong peak at high wavenumbers that is emphasized by the logarithmic scaling and the fact that only little variations are associated with small scales, so that relative changes here turn out to be large. The use of nearest-neighbor interpolation would create the impression of a build-up of power close to the cut-off scale of the grid, when they are actually an imprint of the discontinuity of the field in the finite volume representation. Such a build-up may be interpreted as a numerical instability, grid noise or insufficient damping of unrealistic small scale grid artifacts rather than an artifact of the interpolation method or the grid discretization itself. Such considerations are especially important if one tries to investigate the effective resolution of a numerical model (see also Soufflet et al., 2016), that is, the minimal resolution at which the model still performs reasonably close to reality. One way to define such a minimal resolution is the wavenumber at which the modeled spectral slope significantly diverges from the expected theoretical and/or observational slope of an idealized or even global simulation. Therefore, one needs to be careful when interpreting the high wavenumber end of an interpolated spectrum for data with steep spectral slopes and should be aware of the consequences of the choice of interpolation method.

The resolution of the interpolated grid does not change the qualitative picture much. Using a lower resolution for the interpolation grid does change the high wavenumber representation slightly (not shown), but the overall shape of the spectrum and the qualitative difference between LEITH and KBACK is not affected. Such a low level sensitivity to both interpolation method and resolution of interpolation grid suggests a robust result for the KE spectra. Furthermore, slightly shifting the offset of the interpolation grid, that is, varying the position of the first grid point and consequently the entire interpolated grid, does also not lead to large changes in the KE spectrum. Only the high wavenumbers, which are affected by the interpolation method as well, are also affected by these slight positional changes of the grid, and the effect is only notable for coarse interpolation grids such as $0.09° = 10$ km (not shown).

Finally, the spectra on the oversampled grid exhibit a partial reflection about the nominal resolution at $2h \approx 34.64$ km. This is especially dominant for nearest-neighbor interpolation where a clear peak occurs at $2h$, after which the spectrum falls off again. Therefore, a meaningful interpretation of the data is only possible up to a wavelength of $2h$ as discussed in Section 2.

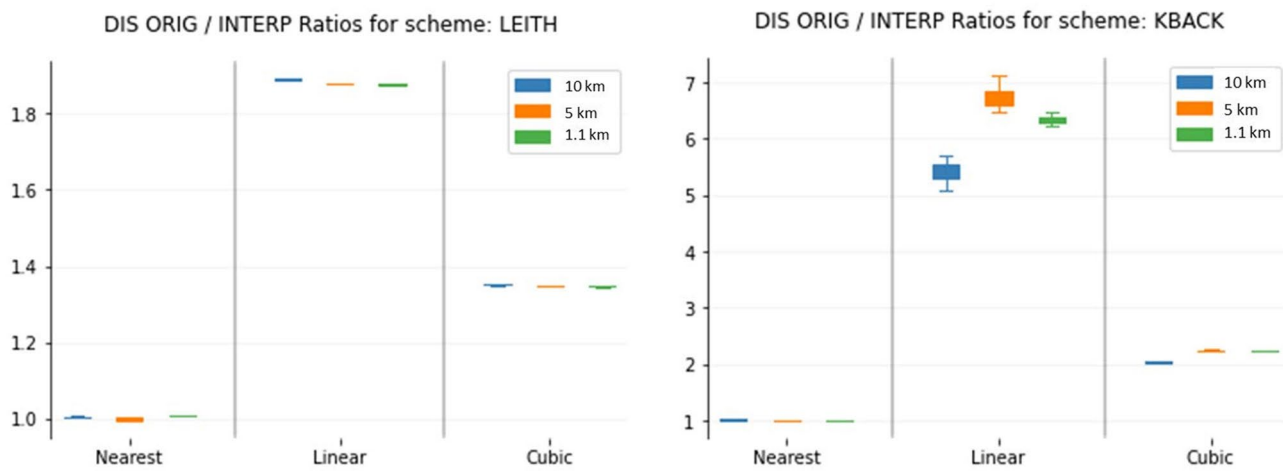

Figure 5. Same as Figure 3 but for total dissipation power. Note the different *y*-axis scaling in the left and right panel. For the kinematic backscatter simulation with the linear and cubic interpolations, only 95% of the days have been used to compute the ratios. Using 100% of the days would increase the spread between different horizontal starting points even more due to some days where the interpolated results are very close to zero or may even switch sign. Removing 5% of the data does not affect the main interpretation of the results.

4.1.2. Dissipation Power Spectra

Dissipation tendencies emphasize, by design, small scales. Consequently, spectra of dissipation power—as a product of velocities and dissipation tendencies—are relatively shallow. Further, dissipation power can be positive or negative. For both of these reasons, dissipation power spectra are displayed on a linear scale.

The methodology is very similar to the KE case. We check that the ratio between the average dissipation power on the triangular grid and the average dissipation power of the sampled interpolated field is close to 1. Figure 5 shows that only nearest-neighbor interpolation passes this test reaching ratios close to 1. All other interpolation schemes are off by at least 30% up to as much as a factor of almost 7. In those cases the interpolated data is not at all representative of the original data and the results are very sensitive to the viscosity operator used in the respective simulations, with substantially larger ratios for KBACK.

The reason for this is that the dissipation tendencies used for the computation of dissipation power have a large grid scale contribution and need to be interpreted in the discontinuous finite volume sense. In the finite volume model FESOM2 the data is always associated to a volume or, at a certain vertical level, to a triangular area. Linear or cubic interpolation, on the other hand, assume that the data is only associated to a specific point and that a smooth curve exists between two neighboring points, which the interpolation tries to estimate. This smoothing leads to a loss of information on fine scales and, as these are important for dissipation tendencies, a loss of information in an overall sense. This problem is also not alleviated when moving to finer interpolation resolution, as the conceptual difference in the interpretation of the finite volume data remains the same.

The effect of interpolation is obvious when looking at actual fields (Figure 6). Interpolation smoothes grid scale fluctuations of dissipation power, but emphasizes row-wise alternating patterns in the meridional direction due to the orientation of the triangles. This issue persists even at a high oversampling ratio, with patterns that depend strongly on the orientation and structure of the grid. It explains how small scale fluctuations project onto large scale structures due to interpolation artifacts. Only nearest-neighbor interpolation retains grid scale fluctuations in both directions, especially for the dissipation tendency contribution, as it actually views the data as discontinuous by construction.

Even though linear and cubic interpolation fail even the first sanity check, it is instructive to look at actual dissipation power spectra for all three interpolation methods (Figure 7). All three methods show that LEITH is dissipative on all scales, while KBACK dissipates on small scales but injects energy on large scale. For Leith, most of the energy is dissipated on large scales due to the fact that most of the kinetic energy can be found at large scales (see Figure 4) and due to the insufficient scale separation between the injection and dissipation scales in these simulations at eddy-permitting resolution. The dissipation operator, while predominantly operating on

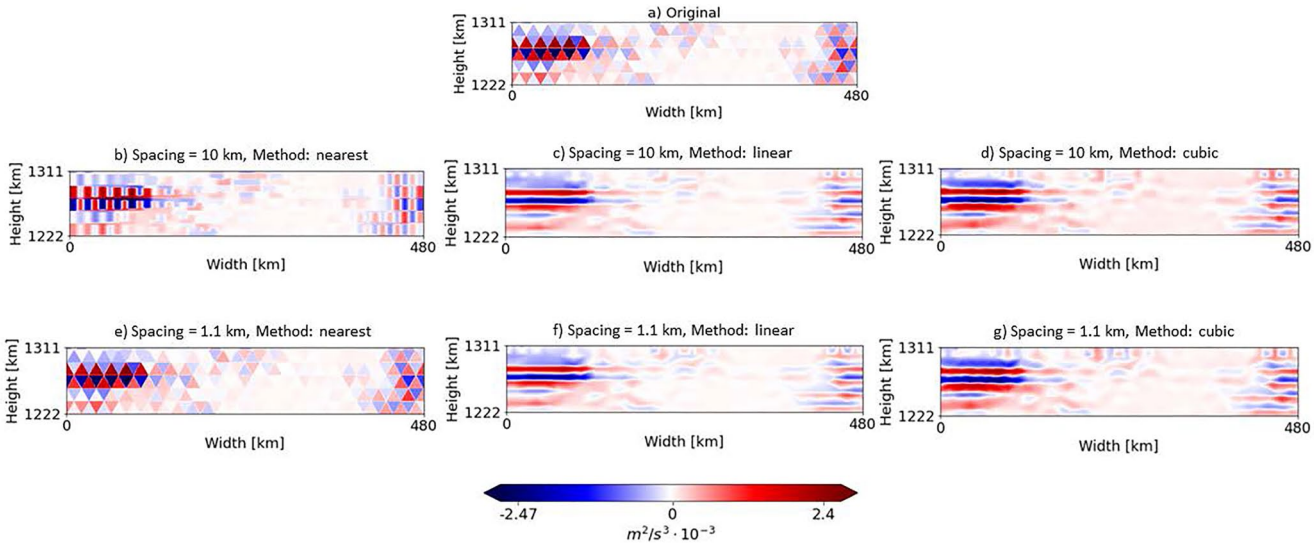

Figure 6. A daily mean of dissipation power for kinematic backscatter (a) on the original triangular grid interpreted in the finite volume sense; after interpolation to a 10×10 km and 1.1×1.1 km grid using nearest neighbor (b and e), linear (c and f) and cubic (d and g) interpolation, respectively. The grid scale structure is only retained by the nearest neighbor interpolation while linear and cubic interpolation lead to smoothing, especially in the zonal direction.

small scales, is therefore also interfering with the large scales which leads to pronounced dissipation at large scales (see, e.g., Juricke et al., 2019; Soufflet et al., 2016). However, only nearest-neighbor interpolation is able to show that there is significant dissipation near the grid scale for both LEITH and KBACK. Worse, linear or cubic interpolated spectra give the impression that the dissipation power in KBACK is predominantly positive, which is physically wrong and numerically impossible.

This example illustrates quite nicely, how an inconsistent interpolation of the data can lead to a quite different and even opposing interpretation of the data. While kinetic energy is expected to be a physically smooth field, such that cubic or linear interpolation are acceptable choices, dissipation power is a field with very low regularity and should be viewed, numerically, as discontinuous and treated in the finite volume framework of the model discretization.

4.2. Resize-and-Average Method

The spectra obtained via the R-a-A method are qualitatively similar to the Fourier spectra (compare Figure 8 with Figures 4 and 7). The results show clearly the distribution of (anti-)dissipation across scales for the backscatter versus the Leith viscosity and the higher levels of KE for KBACK.

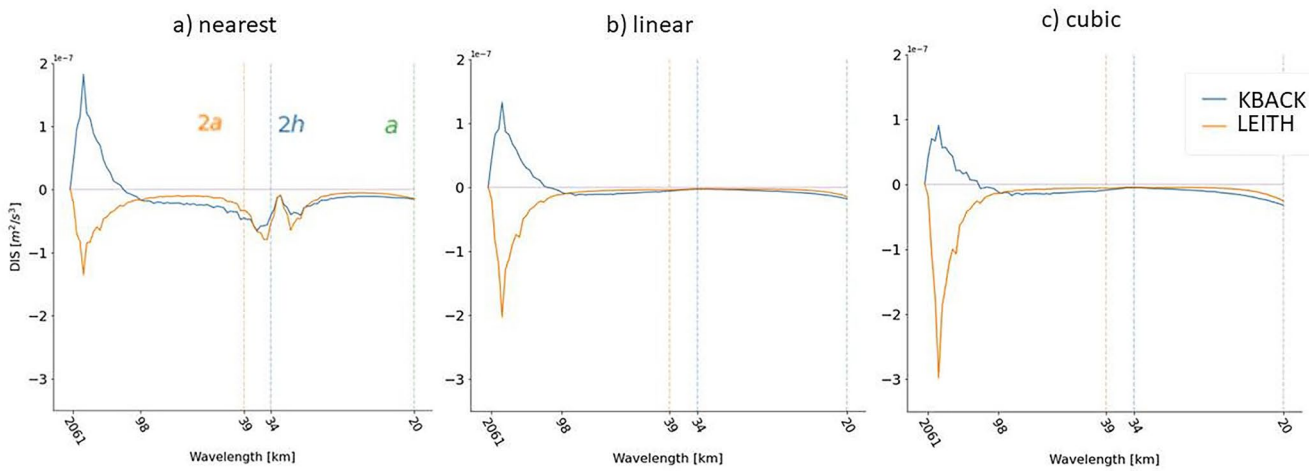

Figure 7. As 4 but for dissipation power spectra. Note the different scaling of the y-axis comapred to 4.

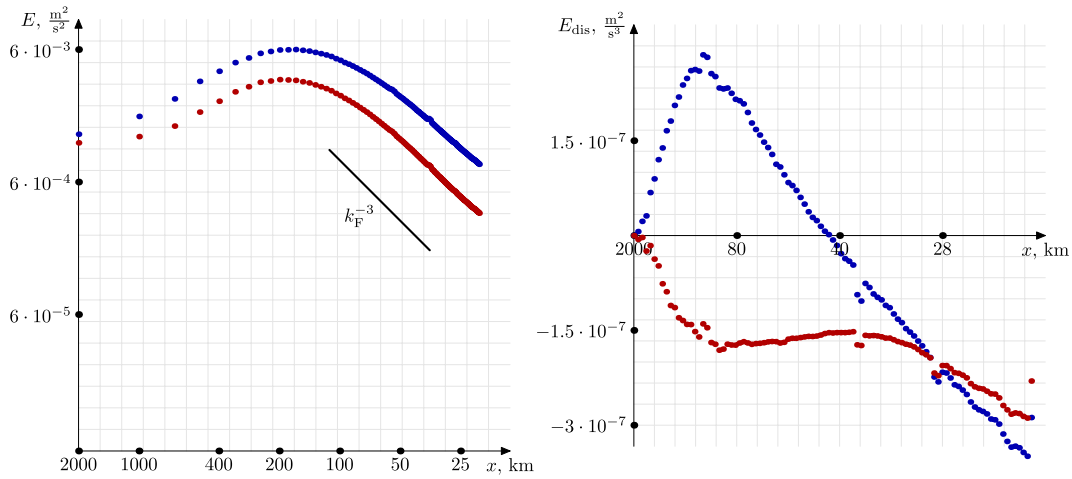

Figure 8. Energy and dissipation power spectra computed by the modified resize-and-average method, see Equations 22 and 23. Blue points correspond to the kinematic backscatter parametrization, red points to the Leith parametrization.

Note that the spectra obtained by Fourier and the modified R-a-A methods are not directly comparable in terms of exact values for specific scales. For example, on equilateral square meshes of the size 100×100, if the spectral slope in the Fourier basis is $-5/3 = -1.66$, then the R-a-A method gives -1.44. For rectangular or triangular meshes of different sizes the R-a-A method may further deviate from the results of Fourier analysis based on interpolated fields. All these aspects are discussed and derived in detail in A. Kutsenko et al. (2022), where the exact correspondence between values computed by Fourier and R-a-A methods is presented. We note that the original R-a-A method determines the energy density for a specific subset of scales $k \sim 2^n$, $n \in \mathbb{N}$ (see A. Kutsenko et al., 2022). The modified R-a-A can recover energy densities for all $k \sim n$. The modified R-a-A method sacrifices orthogonality of subdomains for a higher spectral resolution, but it retains aspects such conservation of domain averages for every domain decomposition due to the nature of the Walsh–Rademacher basis. However, the difference between the slopes in the modified R-a-A and Fourier methods is more noticeable than in the original R-a-A. For the spectral slope k_F^{-3} in the Fourier basis, the modified R-a-A gives a two times smaller slope as determined via preliminary idealized tests (not shown). The theoretical underpinning of the modified R-a-A is a topic of ongoing research.

One should refrain from directly comparing the scale diagnostics based on Fourier and R-a-A analysis. It is more reasonable to compare the results made by the same method for different simulations. In that case, the qualitative characteristics appearing in spectral diagnostics of LEITH and KBACK are the same for both methods. Another significant difference between Fourier and R-a-A diagnostics lies in the interpretation of scales and actual amplitudes. In particular, the resolution x in the original R-a-A method is about twice smaller than the corresponding wavelength in the Fourier method, as we compare indicator functions with sine and cosine functions. Unsurprisingly, it diverges from Fourier analysis quantitatively, as it relies on scale averaging rather than trigonometric separation of the flow.

The R-and-A method can be readily applied to any type of unstructured data and does not suffer from the interpolation issue we faced for dissipation power as it always interprets the data in a finite volume sense. But one needs to be aware of the grid resolution to estimate the maximum resolved wavenumber. Analyzing grid scales becomes difficult, as the averaging operation is most effective for subsets with sufficiently many samples inside.

4.3. Spectra via Discrete Spatial Filtering

We applied the smoothing filter method of Section 2.5 specifically to dissipation power to look at the grid scale differences between LEITH and KBACK (Figures 9 and 10). We first look at the original field and compare it to the local distribution of dissipation power after applying several smoothing filters C and X to see the instantaneous spatial distribution of dissipation on larger scales (Figure 9). While the original field is strongly influenced by the grid scale structure of the data, consecutive smoothing cycles reduce the effect of the grid scales and highlight the differential behavior of LEITH compared to KBACK on larger scales. While LEITH remains

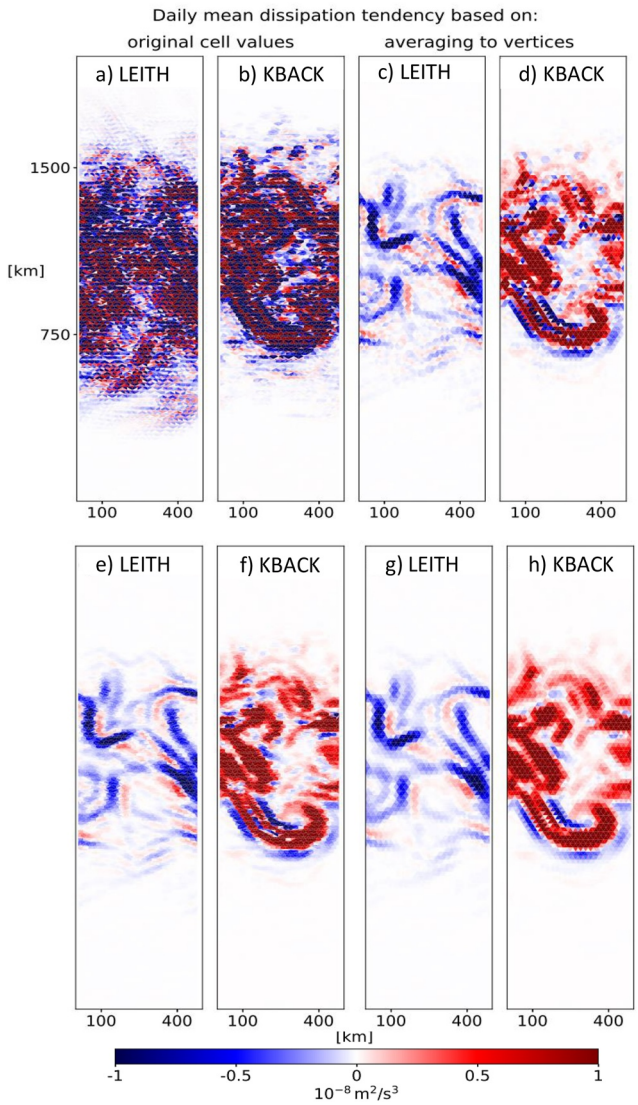

Figure 9. A daily mean of dissipation power on (a + b) the original data, (c + d) after applying the smoothing filter X to velocity and dissipation tendency component before evaluating the scalar product, (e + f) after applying F = CX, and (g + h) after applying XCX for the simulations with (a + c + e + g) Leith and (b + d + f + h) kinematic backscatter parameterization.

dissipative on large scales with negative contributions dominating the dissipation power, KBACK switches sign from mostly negative to positive after applying the filters. This illustrates that backscatter tends to dissipate at small scales, while it injects energy at large scales. Furthermore, it demonstrates the sensitivity of overall dissipation to just one single smoothing cycle and, therefore, the importance to retain small scales when using interpolation for Fourier analysis. The smoothing filter diagnostic also does not only provide an area averaged picture, but highlights the instantaneous regions of strong dissipation or backscatter.

Averaging over the entire model domain for each smoothing cycle and then taking the differences of consecutive smoothing cycles confirms this impression (Figure 10). While LEITH stays dissipative for all differences, that is, for all scale ranges, KBACK actually switches from negative to positive already after only one smoothing cycle (Figure 10). This provides a qualitative illustration of the grid scale behavior of these two methods. However, one can also see that after several smoothing cycles, the dissipation power for both simulations asymptotically tends to zero for large scales. This is due to the fact that the smoothing operation is not orthogonal and therefore does not clearly separate scales. After each iteration of the smoothing filter, more and more large scales are mixed into the small scales and are removed. This is why we can, with the current choice of smoothing filter, only apply the filter method to directly compare two sets of simulations on the same mesh. Further extension in the spirit of the previous section with the orthogonal Walsh–Rademacher basis can be developed from here on. However, we want to stress that the main goal of this specific method is the clear focus on the model grid scale in the context of effective resolution (Soufflet et al., 2016), while the other R-a-A method predominantly focuses on slightly larger up to the largest scales.

5. Conclusion

In this study we investigated several different methods with which to do scale analysis of kinetic energy and dissipation power on the triangular quasi B-grid of the FESOM2 model. Due to the triangular structure and the placement on centroids, the amount of velocity points is about twice the amount of scalar points. In the specific idealized structured triangular grid we consider in this first study, there are two sets of translationally invariant triangle types, one with upward and one with downward pointing triangles. Consequently, a classical spectral Fourier analysis as a simple 2D spectrum is not fully sufficient. We are effectively dealing with an external mode of variability defined by a rhombus as a unit cell and an internal mode controlled by the two triangles with opposite orientation that make up the rhombus.

As alternative pathways to the relatively elaborate full diagnostic of two separate spectra necessary to describe both modes of variability, we present different methods: (a) a spectral analysis on interpolated fields; (b) an alternative scale analysis based on subdomain averaging; (c) a small scale analysis based on successive applications of smoothing filters.

We apply the methods to two sets of data based on a zonally periodic channel for simulations of a primitive equation flow on an equilateral triangular grid with FESOM2. The first data set uses a classical viscous closure. The second one uses a KBACK closure introduced by Juricke, Danilov, Koldunov, Oliver, Sein, et al. (2020).

For the first method, that is, 2D spectral analysis on interpolated fields, one needs to choose both the resolution of the interpolated grid as well as the interpolation method. Oversampling with a finer interpolation grid is necessary to capture the structure of the original triangular grid up its nominal resolution.

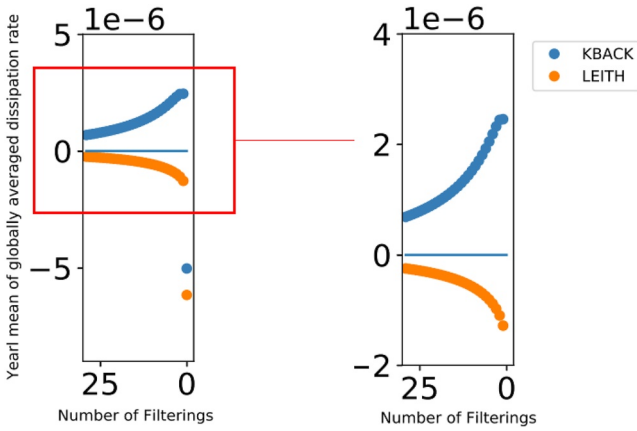

Figure 10. Scale distribution of dissipation power based on globally averaged difference between consecutive smoothing cycles of F = CX (such that data is always placed on centroids) (a) including the original data point without smoothing (i.e., 0 smoothing cycles) and (b) without the original data point.

Regarding the interpolation method, the result is, depending on the investigated field, sensitive to the actual choice. As a first sanity check, one can compute the ratio between the total area-weighted field on the original grid and on the interpolated grid. If these two differ by more than a few percent, the respective interpolation method should not be used. While this first test suggests that all three tested interpolation methods - nearest neighbor, linear and cubic splines—can be used for kinetic energy, only nearest neighbor interpolation should be considered for dissipation power. This is related to the smoothness of the respective fields and the interpretation of the model data. While kinetic energy is expected to have a certain degree of smoothness in the framework of the theory of geostrophic turbulence, dissipation power, due to its relation to numerical dissipation tendencies, is effectively discontinuous in the finite volume discretization of FESOM2. Consequently, oversampling via nearest neighbor interpolation stays close to the original data. This is also visible in the actual spectra for all three methods. The dissipation power spectra is most sensibly represented by nearest neighbor interpolation, while it leads for linear and cubic interpolation to wrong results for KBACK and LEITH, most noticeable, however, for the data of KBACK. In those simulations, all three methods suggest energy injection at large scales and energy dissipation at small scales, as expected. However, only nearest neighbor interpolation shows sufficient dissipation at small scales, while linear and cubic interpolation actually suggest too little dissipation at small scales and overall.

Looking at kinetic energy spectra, the three different interpolation methods provide very similar results. The kinetic energy backscatter simulation has more energy on all scales compared to the classical viscous closure. Differences between the three interpolation methods only appear close to the maximum resolved wavenumber. Here, linear and cubic retain a negative slope, while nearest neighbor emphasizes the small scales and therefore leads to a small build-up of energy near the grid scale. This build-up is visible due to the small amount of total energy at small scales, so that a small increase in energy at those scales leads to a magnified signal in the spectrum. All three interpolation methods provide reasonable spectra, and their difference lies in the interpretation of the data as either a sampling of a naturally smooth field (linear or cubic) or the discontinuous interpretation of the finite volume discretization (nearest neighbor). Consequently, the high wavenumber end of the kinetic energy spectrum should be interpreted with caution.

As our second method, the alternative R-a-A scale analysis based on subdomain averaging introduced by A. Kutsenko et al. (2022) is not directly comparable with Fourier analysis in a quantitative sense. The spectral slopes produced by the R-a-A and the Fourier methods differ. The relationship between the spectral slopes of the two methods is analyzed in detail by A. Kutsenko et al. (2022). Furthermore, the scales in the R-a-A method and the wavelengths of Fourier analysis are different. The difference in scales is about a factor 2: a wavelength in Fourier analysis contains two peaks of the wave, a selected scale in the R-a-A method, however, only contains one peak. Nevertheless, the R-a-A method reproduces the general shape of the kinetic energy and the dissipation power spectrum found with the Fourier spectral method on interpolated grids. The big advantage of the R-a-A method is that it does not depend on the regularity of the mesh and can be easily extended to fully unstructured meshes. Such meshes and data will be investigated in more detail in follow-up studies. However, scales and amplitudes are not directly comparable between a Fourier spectrum and the R-a-A scale analysis, as, for example, the scales for R-a-A correspond to scales of at least twice the size in Fourier analysis. The R-a-A method, however, does not directly allow to investigate grid scale behavior with high accuracy, as the elements of each subdomain become fewer and fewer close to the grid scale.

In follow-up studies, we will apply selected methods to both regular and fully unstructured grids and use them to more closely investigate aspects of different momentum closures and flow simulations. In principle, the R-a-A method can be extended to fully unstructured grids by choosing an adequate decomposition of the domain. Slight variations to this choice of decomposition can then also account for uncertainties related to the area-averaging that constructs the Walsh-Rademacher basis. However, the effect of such choices and the process for an adequate representation of uncertainty will need to be investigated further. One important aspect in this context is the maximum resolved wavenumber of an unstructured grid. Ideally we would aim for the highest resolution, that is,

the smallest triangles of the unstructured grid. How this can be theoretically and rigorously defined and derived is also an open question. However, it is unlikely that any method can achieve this highest resolution, as the sample size of such small triangles in a mesh with widely varying resolution is potentially small and localized, which means that a domain decomposition for the R-a-A method as well as the oversampling and interpolation for the Fourier transformation will introduce an aliasing of the high wavenumbers. Local filters following ideas of Aluie (2019), Grooms et al. (2021) may be better suited due to their local stencils, but they involve some arbitariness that may be hard to remove and may have issues with grid scale patterns that appear in dissipation power. This needs to be explored and compared to results of other methods in the future. Extensions to global meshes as is classically done via spherical harmonics (e.g., Wieczorek & Meschede, 2018) will also need some further work. However, the R-a-A method is generally applicable to arbitrary domains if one takes into account specific spherical projections and uses suitable subdomains. How to best define such subdomains and whether the method is sensitive to the choice of subdomains, remains an open question at this point.

To analyze grid scale behavior in a local sense and especially for dissipation power, the third and final method presented here utilizes a smoothing operator acting on the grid scale, with successive iterations of the filter removing the contribution from small scales. However, as this operator does not divide the domain into orthogonal subsets (contrary to the R-a-A method), successive applications of the filter tend to mix scale contributions. This does not present a substantial issue, though, if only grid scales are of interest, for which a few smoothing cycles are already sufficient.

In general, the methods described and tested in this study tend to complement each other. Due the complex structure of the grid, the violation of translational invariance of the triangular cells and a unit cell being defined by two triangular cells and therefore creating an internal mode of variability, we cannot expect to get a good description of the scale behavior of the flow with just one diagnostic. We need to rely on the combination of different diagnostics. As a note of caution, one should be aware that interpolation can lead to inaccurate or simply wrong results for spectra, depending on the fields under consideration. One needs to carefully choose an adequate interpolation method or a different diagnostic altogether, such as the R-a-A method suggested here.

Data Availability Statement

The model data is publicly available at https://doi.org/10.5281/zenodo.7401541 (Juricke, 2022). The latest stable FESOM2 release is available at https://github.com/FESOM/fesom2. The scripts for the R-a-A method are available at https://doi.org/10.5281/zenodo.7270043 (A. A. Kutsenko, 2022). Routines for the Fourier spectra are available at http://doi.org/10.5281/zenodo.7270305 (Bellinghausen, 2022).

Acknowledgments
We thank the editor and three anonymous reviewers for their insightful comments which helped us to clarify the presentation and to put the results into a broader context. This work is a contribution to projects M3 and S2 of the Collaborative Research Centre TRR 181 "Energy Transfer in Atmosphere and Ocean" funded by the Deutsche Forschungsgemeinschaft (DFG, German Research Foundation) under project number 274762653. The computational resources were supplied by the supercomputing facilities at the Alfred Wegener Institute in Bremerhaven.

References

Aluie, H. (2019). Convolutions on the sphere: Commutation with differential operators. *GEM-International Journal on Geomathematics*, *10*(1), 9. https://doi.org/10.1007/s13137-019-0123-9

Aluie, H., Hecht, M., & Vallis, G. K. (2018). Mapping the energy cascade in the North Atlantic Ocean: The coarse-graining approach. *Journal of Physical Oceanography*, *48*(2), 225–244. https://doi.org/10.1175/jpo-d-17-0100.1

Bachman, S. D., Fox-Kemper, B., & Pearson, B. (2017). A scale-aware subgrid model for quasi-geostrophic turbulence. *Journal of Geophysical Research: Oceans*, *122*(2), 1529–1554. https://doi.org/10.1002/2016jc012265

Bellinghausen, K. (2022). Spectral diagnostics for triangular meshes (Version 1.0) [Software]. Zenodo. https://doi.org/10.5281/zenodo.7270305

Berloff, P. (2018). Dynamically consistent parameterization of mesoscale eddies. Part III: Deterministic approach. *Ocean Modelling*, *127*, 1–15. https://doi.org/10.1016/j.ocemod.2018.04.009

Chen, C., Liu, H., & Beardsley, R. C. (2003). An unstructured, finite volume, three-dimensional, primitive equation ocean model: Application to coastal ocean and estuaries. *Journal of Atmospheric and Oceanic Technology*, *20*(1), 159–186. https://doi.org/10.1175/1520-0426(2003)020<0159:augfvt>2.0.co;2

Danilov, S., Juricke, S., Kutsenko, A., & Oliver, M. (2019). Toward consistent subgrid momentum closures in ocean models. In C. Eden & A. Iske (Eds.), *Energy transfers in Atmosphere and Ocean* (pp. 145–192). Springer-Verlag.

Danilov, S., & Kutsenko, A. (2019). On the geometric origin of spurious waves in finite-volume discretizations of shallow water equations on triangular meshes. *Journal of Computational Physics*, *398*, 108891. https://doi.org/10.1016/j.jcp.2019.108891

Danilov, S., Sidorenko, D., Wang, Q., & Jung, T. (2017). The finite-volume Sea ice–Ocean Model (FESOM2). *Geoscientific Model Development*, *10*(2), 765–789. https://doi.org/10.5194/gmd-10-765-2017

Fox-Kemper, B., & Menemenlis, D. (2008). Can large eddy simulation techniques improve mesoscale rich ocean models? In M. W. Hecht & H. Hasumi (Eds.), *Ocean modeling in an eddying regime* (pp. 319–337). American Geophysical Union.

Fringer, O. B., Gerritsen, M., & Street, R. L. (2006). An unstructured-grid, finite-volume, nonhydrostatic, parallel coastal ocean simulator. *Ocean Modelling*, *14*(3–4), 139–173. https://doi.org/10.1016/j.ocemod.2006.03.006

Grooms, I., Loose, N., Abernathey, R., Steinberg, J. M., Bachman, S. D., Marques, G., et al. (2021). Diffusion-based smoothers for spatial filtering of gridded geophysical data. *Journal of Advances in Modeling Earth Systems*, *13*(9), e2021MS002552. https://doi.org/10.1029/2021ms002552

Jansen, M. F., & Held, I. M. (2014). Parameterizing subgrid-scale eddy effects using energetically consistent backscatter. *Ocean Modelling*, *80*, 36–48. https://doi.org/10.1016/j.ocemod.2014.06.002

Jansen, M. F., Held, I. M., Adcroft, A. J., & Hallberg, R. (2015). Energy budget-based backscatter in an eddy permitting primitive equation model. *Ocean Modelling*, *94*, 15–26. https://doi.org/10.1016/j.ocemod.2015.07.015

Juricke, S. (2022). FESOM2 channel data [Dataset]. Zenodo. https://doi.org/10.5281/zenodo.7401541

Juricke, S., Danilov, S., Koldunov, N., Oliver, M., Sein, D. V., Sidorenko, D., & Wang, Q. (2020). A kinematic kinetic energy backscatter parametrization: From implementation to global ocean simulations. *Journal of Advances in Modeling Earth Systems*, *12*, e2020MS002175. https://doi.org/10.1029/2020ms002175

Juricke, S., Danilov, S., Koldunov, N. V., Oliver, M., & Sidorenko, D. (2020). Ocean kinetic energy backscatter parametrization on unstructured grids: Impact on global eddy-permitting simulations. *Journal of Advances in Modeling Earth Systems*, *12*(1), e2019MS001855. https://doi.org/10.1029/2019ms001855

Juricke, S., Danilov, S., Kutsenko, A., & Oliver, M. (2019). Ocean kinetic energy backscatter parametrizations on unstructured grids: Impact on mesoscale turbulence in a channel. *Ocean Modelling*, *138*, 51–67. https://doi.org/10.1016/j.ocemod.2019.03.009

Khatri, H., Sukhatme, J., Kumar, A., & Verma, M. K. (2018). Surface ocean enstrophy, kinetic energy fluxes, and spectra from satellite altimetry. *Journal of Geophysical Research: Oceans*, *123*(5), 3875–3892. https://doi.org/10.1029/2017jc013516

Kittel, C. (2004). *Introduction to solid state physics* (8th ed.). Wiley.

Klöwer, M., Jansen, M. F., Claus, M., Greatbatch, R. J., & Thomsen, S. (2018). Energy budget-based backscatter in a shallow water model of a double gyre basin. *Ocean Modelling*, *132*, 1–11. https://doi.org/10.1016/j.ocemod.2018.09.006

Korn, P. (2017). Formulation of an unstructured grid model for global ocean dynamics. *Journal of Computational Physics*, *339*, 525–552. https://doi.org/10.1016/j.jcp.2017.03.009

Kumar, P., & Foufoula-Georgiou, E. (1997). Wavelet analysis for geophysical applications. *Review of Geophysics*, *35*(4), 385–412. https://doi.org/10.1029/97rg00427

Kutsenko, A., Danilov, S., Juricke, S., & Oliver, M. (2022). On the relation between Fourier and Walsh–Rademacher spectra for isotropic random fields. Submitted to Elsevier. Retrieved from https://papers.ssrn.com/sol3/papers.cfm?abstract_id=4207464.%20(preprint

Kutsenko, A. A. (2022). Resize and average method (Version 1.0) [Software]. Zenodo.https://doi.org/10.5281/zenodo.7270043

Leith, C. E. (1996). Stochastic models of chaotic systems. *Journal of Physics* D, *98*(2–4), 481–491. https://doi.org/10.1016/0167-2789(96)00107-8

Patching, S. (2022). On divergence- and gradient-preserving coarse-graining for finite volume primitive equation ocean models. *Ocean Modelling*, *170*, 101941. https://doi.org/10.1016/j.ocemod.2021.101941

Pearson, B., Fox-Kemper, B., Bachman, S., & Bryan, F. (2017). Evaluation of scale-aware subgrid mesoscale eddy models in a global eddy-rich model. *Ocean Modelling*, *115*, 42–58. https://doi.org/10.1016/j.ocemod.2017.05.007

Perezhogin, P. (2019). Deterministic and stochastic parameterizations of kinetic energy backscatter in the NEMO ocean model in double-gyre configuration. *IOP Conference Series: Earth and Environmental Science*, *386*(1), 012025. https://doi.org/10.1088/1755-1315/386/1/012025.).

Ruiz-Antolín, D., & Townsend, A. (2018). A nonuniform Fast Fourier Transform based on low rank approximation. *SIAM Journal on Scientific Computing*, *40*(1), A529–A547. https://doi.org/10.1137/17m1134822

Sadek, M., & Aluie, H. (2018). Extracting the spectrum of a flow by spatial filtering. *Physical Review Fluids*, *3*(12), 124610. https://doi.org/10.1103/physrevfluids.3.124610

Schubert, R., Gula, J., Greatbatch, R. J., Baschek, B., & Biastoch, A. (2020). The submesoscale kinetic energy cascade: Mesoscale absorption of submesoscale mixed layer eddies and frontal downscale fluxes. *Journal of Physical Oceanography*, *50*(9), 2573–2589. https://doi.org/10.1175/jpo-d-19-0311.1

Smagorinsky, J. (1963). General circulation experiments with the primitive equations: I. The basic experiment. *Monthly Weather Review*, *91*(3), 99–164. https://doi.org/10.1175/1520-0493(1963)091<0099:gcewtp>2.3.co;2

Soufflet, Y., Marchesiello, P., Lemarié, F., Jouanno, J., Capet, X., Debreu, L., & Benshila, R. (2016). On effective resolution in ocean models. *Ocean Modelling*, *98*, 36–50. https://doi.org/10.1016/j.ocemod.2015.12.004

Storer, B. A., Buzzicotti, M., Khatri, H., Griffies, S. M., & Aluie, H. (2022). Global energy spectrum of the general oceanic circulation. *Nature Communications*, *13*(1), 5314. https://doi.org/10.1038/s41467-022-33031-3

Wang, S., Qiao, F., Dai, D., & Zhou, X. (2019). Anisotropy of the sea surface height wavenumber spectrum from altimeter observations. *Scientific Reports*, *9*(1), 15896. https://doi.org/10.1038/s41598-019-52328-w

Wieczorek, M. A., & Meschede, M. (2018). SHTools: Tools for working with spherical harmonics. *Geochemistry, Geophysics, Geosystems*, *19*(8), 2574–2592. https://doi.org/10.1029/2018gc007529

Zhang, Y. J., Ye, F., Stanev, E. V., & Grashorn, S. (2016). Seamless cross-scale modeling with SCHISM. *Ocean Modelling*, *102*, 64–81. https://doi.org/10.1016/j.ocemod.2016.05.002